

CFD-DEM study of mixing in a monodispersed solid-liquid fluidized bed

Victor Oliveira Ferreira^{a,c}, Bruno Blais^c, Gabriela Cantarelli Lopes^{a,b,*}

^a*Chemical Engineering Graduate Program, Federal University of São Carlos, Rod. Washington Luiz, Km 235 - SP 310, São Carlos, SP 13565-905, Brazil*

^b*Chemical Engineering Department, Federal University of São Carlos, Rod. Washington Luiz, Km 235 - SP 310, São Carlos, SP 13565-905, Brazil*

^c*Chemical engineering High-performance Automatization Optimization and Simulation (CHAOS), Department of Chemical Engineering, Polytechnique Montréal, PO Box 6079, Stn Centre-Ville, Montréal, QC, Canada, H3C 3A7*

Abstract

In this work, we assess the internal dynamics of particles in liquid-solid fluidized beds using an unresolved CFD-DEM model. We use the Nearest Neighbors Method (NNM) and the mixing index based on the principal component analysis proposed by Doucet et al. [1] to quantify the bed mixing for several flow regimes and particle properties. Discussions on the advantages and drawbacks of each method are provided. Using results for several inlet flow rates, we show that the dimensionless mixing time reaches a plateau and does not increase significantly with the inlet velocity. The principal component analysis shows that the studied fluidized bed has no preferential mixing component. Additionally, we show that, except for the sliding friction coefficient, the collision properties have almost negligible influence on the mixing behavior.

Keywords: Liquid-solid fluidized bed (LSFB), Unresolved CFD-DEM, FEM-DEM, Multiphase flow.

*Corresponding author.

Email address: gclopes@ufscar.br (Gabriela Cantarelli Lopes)

1. Introduction

Liquid-solid fluidized beds (LSFB) are applicable to various processes in which enhanced heat and/or mass transfer between particles and liquids are desired [2]. In these equipment, the drag force counterbalances the apparent mass of the particles, agitating particles in a dynamically stable and uniform fluidized state [3]. Though the interphase momentum exchange plays the most important role in the fluidization state, the collisions between particles are an important part of the fluidization dynamics and should be taken into account. Anaerobic fluidized bed reactors (AFBRs), for example, rely on uniform fluid-particle and particle-particle interactions through the equipment's volume to control the removal rate of the treated matter from the particle's surface, consequently, mixing plays an important role in the process's efficiency [4].

Measuring the degree of mixing of particles *in-situ* is not trivial, especially in liquid-particle systems. It is challenging to track the movement of individual particles, and, consequently, detect abnormal distributions of particles or inefficient mixing through the equipment's volume.

One alternative to studying the mixing behavior in liquid-solid systems avoiding experimental limitations is to use simulations. The unresolved Computational Fluid Dynamics-Discrete Elements Method (CFD-DEM) [5; 6], validated to several fluid-particle systems [7–11], stands out for being able to simulate fluid-particle and particle-particle interactions in systems with hundreds of thousands of particles at a reasonable computational cost [6; 12].

The unresolved CFD-DEM is particularly powerful in the study of particles' mixing compared to other approaches, such as the Two-Fluid Model (TFM), since the DEM allows for individual particle tracking [12]. Knowing the positions of particles over time allows the use of several methods for mixing measurement, including variance reduction ratio [13], nearest neighbors method (NNM), neighbor distance method, Average height method [14], mixing entropy [15], mixing segregation index [16], Lacey mixing index [17], Doucet mixing index [1], and others [18].

In these methods, mixing is expressed as an index varying between 0 (for unmixed systems) and 1 (for fully mixed systems). Usually, the system is considered fully mixed when the mixing index is > 0.90 , and the time it takes for the value to be achieved (t_{90}) is used to express mixing time, allowing for the comparison between mixing methods, regimes, and equipment designs. Recently, we have validated the unresolved CFD-DEM method [11] against liquid-solid fluidized bed experiments [19] at a wide range of flow regimes. However, to the best of our knowledge, unresolved CFD-DEM was not used to study the mixing of particles within the bed. In fact, few studies on mixing in liquid-solid fluidized beds have been reported, and most of those efforts focus on bidisperse systems [20–24].

Given the importance of solid agitation and mixing for the conversion in liquid-solid reactors and given the lack of reports on the matter, in this work, we assess the mixing behavior of particles in a liquid-solid fluidized bed using techniques based on the discrete information of particles obtained from unresolved CFD-DEM simulations. To do so, we measure the degree of mixing of three different monodispersed beds at a wide range of regimes (Re from 534 to 19021) using NNM [14] and the mixing index by Doucet et al. [1]. We discuss the effect of the regime on the mixing time and assess the principal component of mixing. Additionally, the role of particles' collisional properties (Young's modulus, coefficient of restitution, sliding and rolling friction) in the mixing behavior was also investigated. Finally, we show the influence of regimes and particle properties on the solid mixing rate.

2. Governing equations

We briefly describe the model formulation used in this work. A full description of the model can be found in previous papers [10; 11; 25–27]. For a more fundamental description of the Volume-Average Navier-Stokes equations, we refer the reader to Zhou et al. [5], Bérard et al. [6], Gidaspow [28], and Geitani et al. [25]; and for the DEM formulation, we refer to Zhu et al. [29], Blais et al.

[30], and Golshan et al. [31].

2.1. Solid phase formulation

For each particle, we apply Newton's second law of motion. The translational and angular components of the momentum are, respectively:

$$m_i \frac{d\mathbf{v}_i}{dt} = \sum_{j=1, j \neq i} (\mathbf{f}_{c,ij}) + \sum_{j, j \neq i} (\mathbf{f}_{nc,ij}) + \mathbf{f}_{pf,i} + \mathbf{f}_g, \quad (1)$$

$$I_i \frac{d\boldsymbol{\omega}_i}{dt} = \sum_{j, j \neq i} (\mathbf{M}_{t,ij} + \mathbf{M}_{r,ij}) \quad (2)$$

where i and j are particles, \mathbf{v} is the particle's velocity, \mathbf{f}_c is the set of contact forces, \mathbf{f}_g is the gravitational force, \mathbf{f}_{pf} the summation of fluid-particle interacting forces, and \mathbf{M}_t and \mathbf{M}_r are the tangential and rolling friction torques.

Particles' collisions are simulated using the soft-sphere model proposed by Cundall and Strack [32]:

$$\mathbf{f}_{c,ij} = \mathbf{f}_{cn,ij} + \mathbf{f}_{ct,ij} = -k_{n,ij} \boldsymbol{\delta}_{n,ij} - \gamma_{t,ij} \dot{\boldsymbol{\delta}}_{n,ij} - k_{t,ij} \boldsymbol{\delta}_{t,ij} - \gamma_{t,ij} \dot{\boldsymbol{\delta}}_{t,ij} \quad (3)$$

where the subscripts n and t mean normal and tangential, respectively. $k_{n,ij}$ and $k_{t,ij}$ are the stiffness, while $\gamma_{n,ij}$ and $\gamma_{t,ij}$ are the damping coefficients of the colliding pair, calculated according to the equations in Table 1.

The tangential and rolling friction torques are calculated, respectively, as:

$$\mathbf{M}_{t,ij} = \mathbf{r}_{i,j} \times (\mathbf{f}_{ct,ij}) \quad (4)$$

$$\mathbf{M}_{r,ij} = -\mu_{r,ij} |\mathbf{f}_{ct,ij}| \frac{\boldsymbol{\omega}_{ij}}{|\boldsymbol{\omega}_{ij}|} R_{ij}^* \quad (5)$$

where the coefficient of rolling friction ($\mu_{r,ij}$) and the equivalent radius (R_{ij}^*) are calculated by the equations in Table 1.

The particle-fluid interaction forces are calculated as:

$$\mathbf{f}_{pf,i} = \mathbf{f}_{d,i} + \mathbf{f}_{\nabla p,i} + \mathbf{f}_{\nabla \cdot \boldsymbol{\tau},i} + \mathbf{f}_{Ar,i} + \mathbf{f}_{\text{Saff},i} \quad (6)$$

Table 1: DEM equations

Property	Equation
Radius of particle i	R_i
Distance from the contact point	$\mathbf{r}_{i,j}$
Equivalent mass	$\frac{1}{m_{ij}^*} = \frac{1}{m_i} + \frac{1}{m_j}$
Equivalent radius	$\frac{1}{R_{ij}^*} = \frac{1}{R_i} + \frac{1}{R_j}$
Equivalent Young's modulus	$\frac{1}{Y_{ij}^*} = \frac{1-\nu_i^2}{Y_i} + \frac{1-\nu_j^2}{Y_j}$
Equivalent shear modulus	$\frac{1}{G_{ij}^*} = \frac{2(2+\nu_i^2)(1-\nu_i^2)}{G_i} + \frac{2(2+\nu_j^2)(1-\nu_j^2)}{G_j}$
Normal stiffness	$k_{n,ij} = \frac{4}{3}Y_{ij}^* \sqrt{R_{ij}^*} \delta_{n,ij}$
Tangential stiffness	$k_{t,ij} = 8G_{ij}^* \sqrt{R_{ij}^*} \delta_{n,ij}$
Normal damping	$\gamma_{n,ij} = -2\sqrt{\frac{5}{6}} \frac{\ln(e)}{\sqrt{\ln^2(e)+\pi^2}} \sqrt{\frac{2}{3}k_{n,ij}m_{ij}^*}$
Tangential damping	$\gamma_{t,ij} = -2\sqrt{\frac{5}{6}} \frac{\ln(e)}{\sqrt{\ln^2(e)+\pi^2}} \sqrt{k_{t,ij}m_{ij}^*}$

where $\mathbf{f}_{d,i}$ is the drag force, $\mathbf{f}_{\nabla p,i}$ is the pressure gradient force, $\mathbf{f}_{\nabla \cdot \boldsymbol{\tau},i}$ is the particle-fluid shear force, and $\mathbf{f}_{\text{Saff},i}$ is the Saffman lift force. Each of these terms is explained in subsection 2.3. Other forces, namely Basset, Magnus, and virtual mass, were neglected [11; 33].

2.2. Liquid phase modeling

The liquid phase in the unresolved CFD-DEM approach is modeled using the Volume-Averaged Navier-Stokes equations (VANS). The model type A [28] (also known as model set II [5]) of the VANS equations is used in the present work [11; 25].

$$\frac{\partial \varepsilon_f}{\partial t} + \nabla \cdot (\varepsilon_f \mathbf{u}) = 0 \quad (7)$$

$$\rho_f \left[\frac{\partial \varepsilon_f \mathbf{u}}{\partial t} + \nabla \cdot (\varepsilon_f \mathbf{u} \otimes \mathbf{u}) \right] = -\varepsilon_f \nabla p + \varepsilon_f \nabla \cdot \boldsymbol{\tau} - \mathbf{F}_{pf} \quad (8)$$

In Eq. (8), $\boldsymbol{\tau}$ is the deviatoric stress tensor

$$\boldsymbol{\tau} = \mu \left[(\nabla \cdot \mathbf{u}) + (\nabla \cdot \mathbf{u})^T - \frac{2}{3} (\nabla \cdot \mathbf{u} \mathbf{I}) \right] \quad (9)$$

where μ is the dynamic viscosity and \mathbf{I} is the identity tensor, and \mathbf{F}_{pf} is the

fluid-particle momentum exchange (source) term

$$\mathbf{F}_{pf} = \frac{1}{\Delta V_{\Omega_C}} \sum_i^{N_{p,C}} (\mathbf{f}_{d,i}) = \frac{1}{\Delta V_{\Omega_C}} \sum_i^{N_{p,c}} (\mathbf{f}_{pf,i} - \mathbf{f}_{\nabla p} - \mathbf{f}_{\nabla \cdot \boldsymbol{\tau}} - \mathbf{f}_{Ar}) \quad (10)$$

where the index $N_{p,C}$ stands for the number of particles inside the cell Ω_C over which the averaging is applied. The force terms in Eq. (10) are the same as in Eq. (6).

2.3. Interphase momentum exchange

In this subsection, the terms in Eqs. (10) and (6) are individually described. Details about each of the terms can be found in Crowe et al. [34].

2.3.1. Undisturbed flow and buoyancy forces

In Lethe, ∇p does not account for the hydrostatic pressure, hence, buoyancy forces ($\mathbf{f}_{Ar,i}$) need to be added separately in Eq. (6). The expressions that represent the pressure gradient and buoyancy forces are, respectively:

$$\mathbf{f}_{\nabla p,i} = V_{p,i} \nabla p \quad (11)$$

$$\mathbf{f}_{Ar,i} = V_{p,i} \rho_f \mathbf{g} \quad (12)$$

where $V_{p,i}$ is the volume of the particle i , ρ_f is the density of the fluid, p stands for dynamic pressure, \mathbf{g} is the gravity acceleration vector. Note that Eq. (11) accounts for the interchange force due to the undisturbed pressure only.

The force resulting from the fluid shear stress is written as:

$$\mathbf{f}_{\nabla \cdot \boldsymbol{\tau},i} = V_{p,i} \nabla \cdot \boldsymbol{\tau} \quad (13)$$

2.3.2. Drag force

The drag force is defined as:

$$\mathbf{F}_d = \sum_i^{N_{p,C}} \mathbf{f}_{d,i} = \sum_i^{N_{p,C}} \beta_i (\mathbf{u} - \mathbf{v}_i) \quad (14)$$

For model A, β_i is the interphase momentum transfer coefficient, given by correlations in the literature [28; 35–38]. The correlation by Rong et al. [38] was applied to all simulations in this work for presenting the best correspondence with the experimental data in the validation campaign [11; 19]. In the correlation, β_i is calculated as:

$$\beta_i = \frac{1}{2} C_{D0} \frac{\pi d_p^2}{4} \rho_f |\mathbf{u} - \mathbf{v}_i| G(\varepsilon_f, \text{Re}_{p,i}) \quad (15)$$

where C_{D0} is the drag coefficient for a single particle, given by the correlation by DallaValle [39]

$$C_{D0} = \left(0.63 + \frac{4.8}{\sqrt{\text{Re}_p}} \right)^2 \quad (16)$$

and $G(\varepsilon_f, \text{Re}_{p,i})$ is

$$G(\varepsilon_f, \text{Re}_{p,i}) = \frac{C_{D,i}}{C_{D0}} = \varepsilon_f^{2 - \left\{ 2.65(\varepsilon_f + 1) - (5.3 - 3.5\varepsilon_f)\varepsilon_f^2 \exp \left[-\frac{(1.5 - \log_{10} \text{Re}_{p,i})^2}{2} \right] \right\}} \quad (17)$$

2.3.3. Saffman lift force

The Saffman lift force is calculated using the Saffman-Mei lift force model, which is a combination of the equations proposed by Saffman [40, 41] and Mei [42]

$$\mathbf{f}_{\text{Saff},i} = 1.161 C_{\text{Saff},i} d_p^2 (\mu \rho_f)^{1/2} |\boldsymbol{\omega}_{c,i}|^{-1/2} [(\mathbf{u} - \mathbf{v}_i) \times \boldsymbol{\omega}_{c,i}] \quad (18)$$

where $\boldsymbol{\omega}_{c,i}$ is the fluid vorticity ($\nabla \times \mathbf{u}$), $C_{\text{Saff},i}$ is the Saffman lift coefficient

$$C_{\text{Saff},i} = \begin{cases} (1 - 0.3314\alpha^{1/2}) \exp\left(\frac{-\text{Re}_{p,i}}{10}\right) + 0.3314\alpha^{1/2}, & \text{for } \text{Re}_{p,i} \leq 40 \\ 0.0524(\alpha_l \text{Re}_{p,i})^{1/2}, & \text{for } \text{Re}_{p,i} > 40 \end{cases} \quad (19)$$

and α is given by:

$$\alpha = \frac{d_p}{2|\mathbf{u} - \mathbf{v}_i|} |\boldsymbol{\omega}_{c,i}| \quad (20)$$

We refer the reader to Crowe et al. [34] for further details on the Saffman lift force model. Previous works show that the Saffman lift force prevents fluid

preferential path through the walls, which are critical to the particle dynamics when simulating liquid fluidized beds [11].

3. Methods

All simulations were carried out using Lethe [10; 25; 26; 31; 43], an open-source CFD/DEM/CFD-DEM tool based on deal.II Finite Elements Method (FEM) library [44; 45]. The methodology applied to this work was previously validated against pilot-scale experimental data by us [19], as described in Ferreira et al. [11]. Lethe’s unresolved CFD-DEM module was also validated for other gas-solid and liquid-solid systems, including fluidized beds, spouted beds, and rotary kilns [10; 27].

3.1. Simulation setup

The simulation setup applied to this work follows what is described in the validation study conducted by our group [11]. We used the pilot-scale circulating liquid-solid fluidized bed described in Ferreira et al. [19] and Ferreira et al. [11] as a reference to the simulations. The experimental unit is composed of a 1 m height, 10 cm diameter cylindrical vessel, where particles are fluidized in water.

Unless mentioned, simulations follow the parameters described in Table 2. Particles’ collisional properties, namely Young’s modulus (Y), coefficient of restitution (e), coefficient of rolling friction (μ_r), and coefficient of sliding friction (μ_f) were the only parameters related to particles modified throughout the study (Section 3.3).

3.1.1. Mesh and initial packing of particles

We used deal.II’s built-in tool to generate the mesh used in all simulations. The mesh is composed of a 1.10 m height, 10 cm diameter cylinder, as shown in Figure 1. The number of elements in cylindrical coordinates ($n_r \times n_\theta \times n_z$) is $6 \times 16 \times 132$. An analysis of the mesh can be found in Ferreira et al. [11].

During simulations, particles are held 10 cm above the bottom of the mesh by a floating wall, leaving a free-of-particles inlet portion to the fluid (referred

Table 2: Simulation parameters.

Parameter	Value
Time integration method	BDF1
CFD time-step and coupling interval (Δt_{CFD})	0.001 s
DEM time-step (Δt_{DEM})	0.000 01 s
Diameter of the cylinder (D_C)	10 cm
Height of the cylinder (H_C)	1.10 m
Height of the inlet portion	10 cm
Mesh ($n_r \times n_\theta \times n_z$)	$6 \times 16 \times 132$
Liquid density (ρ_f)	996.78 kg m^{-3}
Liquid dynamic viscosity (μ)	$8.352 \times 10^{-4} \text{ Pa s}$
Young's modulus (Y)	10 MPa
Coefficient of restitution (e)	0.9
Poisson ratio (ν)	0.3
Coefficient of rolling friction (μ_r)	0.2
Coefficient of sliding friction (μ_f)	0.1
VANS model type	A
Void fraction calculation scheme	PCM
Void fraction smoothing length	$2.0 \times d_p$
Boundary conditions at the walls	Free slip
Drag model	Rong et al. [38]
Lift force model	Saffman-Mei ¹
Gravity (g)	9.81 m s^{-2}

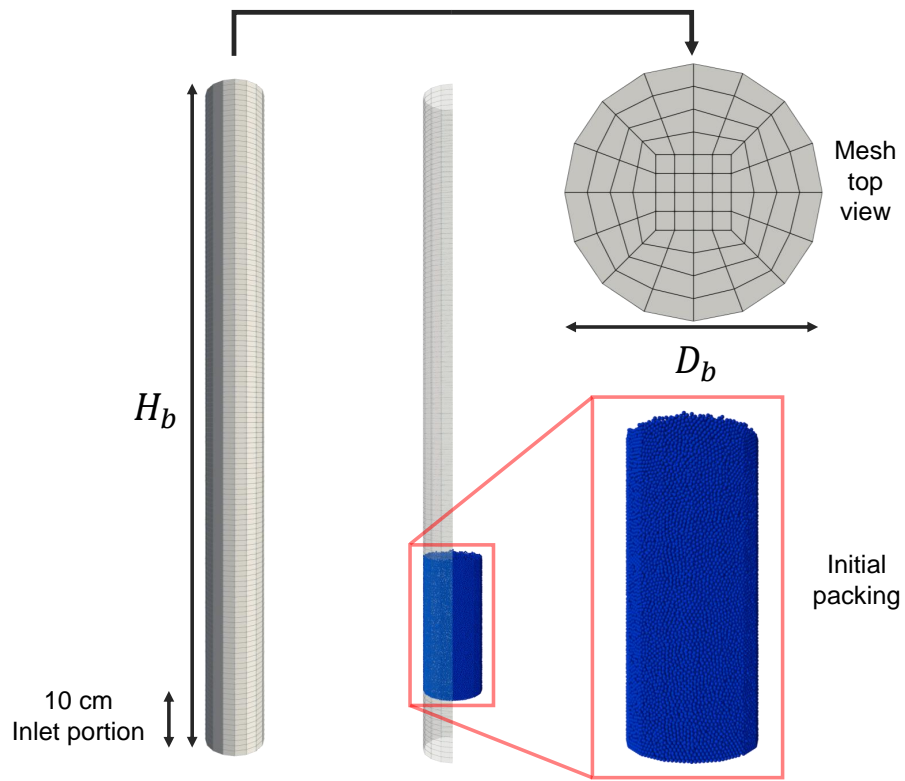


Figure 1: Schematic representation of the mesh and initial packing of particles.

to as inlet portion in Figure 1), preventing sharp void fraction changes in the proximity of the boundaries, which can lead to numerical instabilities [25]. In all simulations, the fluid injection only starts after particles are fully settled above the floating wall. This is achieved by running a DEM simulation, carried out on Lethe-DEM [31], prior to the CFD-DEM simulation.

3.1.2. Particles

We used 3 different groups of particles, named A, B, and C. Particles A and C are referred to as "alginate" and "alumina" in the validation study [11], as shown in Figure 2. For particles A and C, the parameters are the same as the experimental study. Since particle C is more than three times denser than particle A, we created a fictitious intermediary particle B with the same size as particle A and a density close to the acrylonitrile butadiene styrene (ABS) particle used in Ferreira et al. [19]. The particular parameters associated with each particle are presented in Table 3.

Table 3: Particle associated parameters.

Parameter	Particle A	Particle B	Particle C
Total real-time of simulations	35 s	20 s	20 s
Mixing index reference time (t_0)	10 s	5 s	5 s
Output time-step (Δt_{DEM})	0.50 s	0.20 s	0.20 s
Number of particles (N_p)	107960	107960	72400
Particle terminal velocity (U_0)	2.9 cm s ⁻¹	20.8 cm s ⁻¹	48.2 cm s ⁻¹
Lowest and highest inlet velocities (U)	0.44 - 1.09 cm s ⁻¹	4.24 - 11.00 cm s ⁻¹	8.50 - 15.70 cm s ⁻¹
Number of inlet velocities	7	2	8
Diameter of the particles (d_p)	2.66 mm	2.66 mm	3.09 mm
Density of the particles (ρ_p)	1029 kg m ⁻³	1822 kg m ⁻³	3586 kg m ⁻³

3.1.3. Validation

The main results of the validation campaign are presented in Figure 2. All results of the validation step were obtained using the parameters in Table 2. In the Figure, the total pressure drop is compared to the analytical pressure drop calculated by [3]:

$$-\Delta p = \frac{M_p (\rho_p - \rho_f) g}{\rho_p A_b} \quad (21)$$

where M_p is the total mass of particles in the bed, ρ_p is particle's density, ρ_f is fluid's density, g is gravity acceleration constant, and A_b is the bed's cross section area. Bed expansion results (expressed as bed average porosity, $\bar{\varepsilon}_f$) are compared to experiments and estimations using the equation by Richardson and Zaki [46] (R-Z). In the figures, α corresponds to a double-tail confidence interval. The simulation results correspond to time averages in the pseudo-steady-state regime, and the error bars are equivalent to one temporal standard deviation.

The results in Figure 2 were obtained for particles A and C (Table 3) using the parameters in Table 2 and the mesh in Figure 1. The simulations were capable of accurately reproducing the fluidized bed behavior. For further details on the importance of the Saffman lift force, the choice of the drag correlation, and the mesh, we refer the reader to Ferreira et al. [11].

3.2. Mixing index

Several methods can be applied to track particles' mixing using DEM information. In this work, we applied two: the nearest neighbors method (NNM) [14; 47] and Doucet's mixing index [1]. Both methods were applied to Lethe-DEM results using a post-processing module written in Python using the PyVista library [48] (available on Lethe's official GitHub webpage, explained in details on Lethe's official documentation). Different from Lacey's mixing index [17; 47], the methods are grid-independent, meaning that only the particle position is required. NNM and Doucet's methods follow different principles, thus, providing different information about the particles mixing.

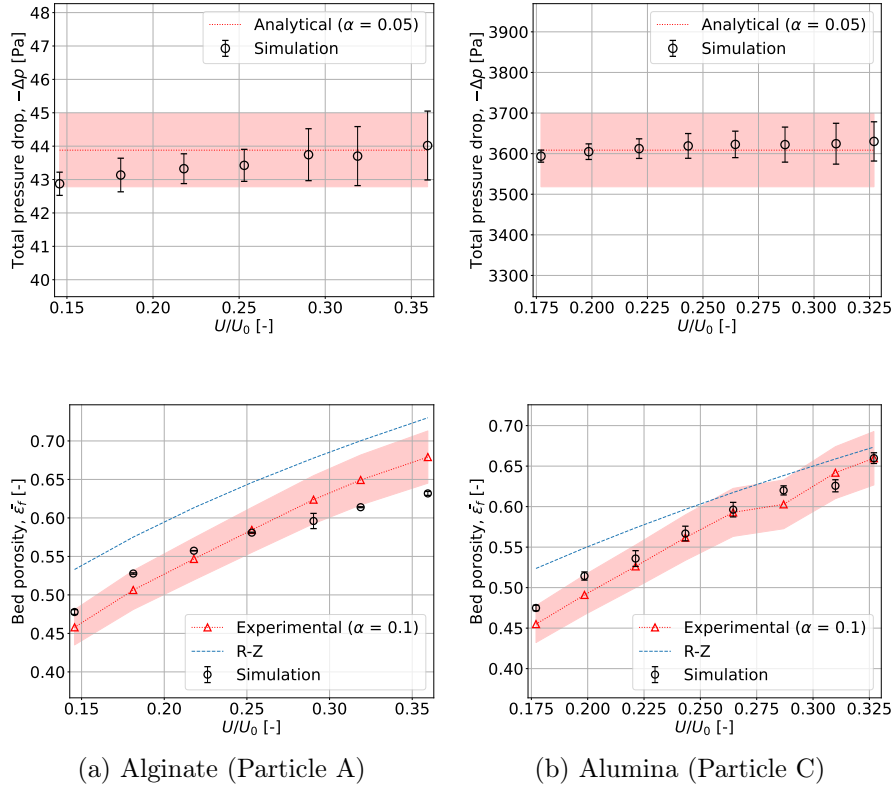


Figure 2: Average of the total pressure difference ($-\Delta p$) and bed expansion ($\bar{\epsilon}_f$) of the validation campaign for the (a) alginate (particle A in this work) and (b) alumina particles (particle C in this work). Adapted from Ferreira et al. [11].

3.2.1. Nearest neighbors method

The method consists of splitting the particles into two groups according to their position at a given moment and tracking the number of neighbors per particle that are part of the other group. A schematic representation of the method is presented in Figure 3.

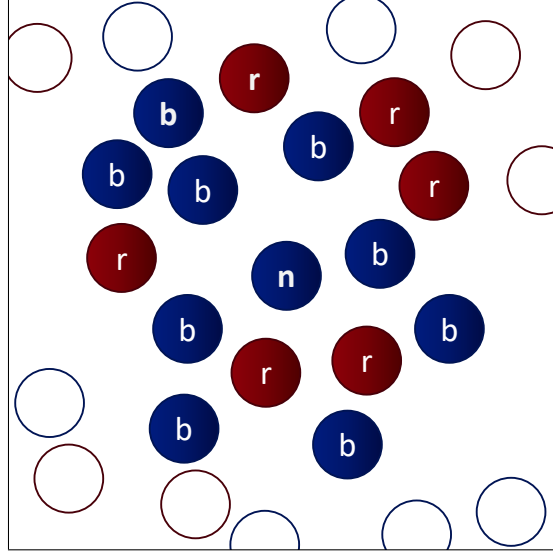


Figure 3: Schematic bi-dimensional representation of the nearest neighbors method for mixing index calculation [47]. In the Figure, blue ("b") and red ("r") particles are members of two different groups. The n^{th} particle, represented by the letter "n" on it, is a blue particle to which the NNM mixing index is calculated. Hollow particles are not part of the 15 nearest neighbors of the particle and, hence, are not used in the mixing index calculation.

The NNM mixing index is calculated by [47] as:

$$\bar{M}_t^{\text{NNM}} = 1/N_p \sum_{n=0}^{N_p} M_n^{\text{NNM}} = 1/N_p \sum_{n=0}^{N_p} \frac{2N_{n,\text{diff}}}{N_{\text{neighbors}}} \quad (22)$$

where \bar{M}_t^{NNM} is the average mixing index of the system at time t , M_n^{NNM} is the mixing index of the n^{th} particle, N_p is the total number of particles in the system, $N_{\text{neighbors}}$ is the number of nearest neighbors used in the method (user-defined parameter), and $N_{n,\text{diff}}$ is the number of neighbor particles that

are of the opposite group of the n^{th} particle. In the present work, we chose $N_{\text{neighbors}} = 15$. The KD-tree nearest neighbors method implemented in the Scikit-learn Python module [49] was used to find particles' nearest neighbors.

In Figure 3, blue and red particles are part of different groups. Filled particles are part of the 15 nearest neighbor particles of particle n , while hollow particles are not. Since $N_{n,\text{diff}}$ is 6 (number of filled red particles), according to Eq. (22), $M_n^{\text{NNM}} = 0.8$. Note that $0 \leq M_n^{\text{NNM}} \leq 2$, so that $0 \leq \bar{M}^{\text{NNM}} \leq 1$.

In NNM, the particles must be split in half so that the coordinate components can be analyzed individually. Since we are working in a cylindrical geometry, particles are split according to their position in cylindrical coordinates (namely r , θ , and z).

The moment of splitting is chosen so that the initial bed expansion, which presents different bed dynamics from the fully expanded pseudo-stationary bed, is not considered. This reference time (t_0) is 10 s for all particles, which is considered the time needed for Particle A to reach the pseudo-steady state [11]. An example of the bed splitting per coordinate is presented in Figure 4.

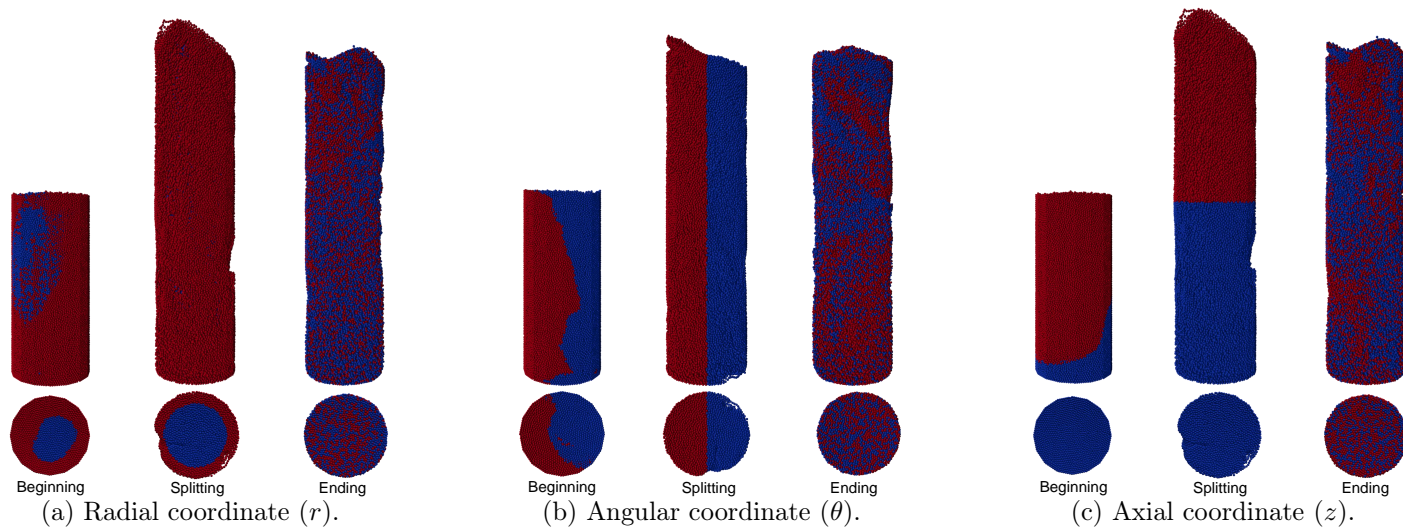


Figure 4: Example of side and bottom views of the beginning, splitting, and ending time-steps of simulations per coordinate. Particles are split according to their position so that NNM can be applied. Splitting directions follow the cylindrical coordinates system, i.e., radius (r), angle (θ), and height (z). Particles are split at the splitting time step such that half of the particles will be part of each group.

As shown in Figure 4, NNM results do not start from zero because, at t_0 , the particles close to the splitting boundary will have neighbor particles on the opposite side. As a consequence, the higher the surface area of the splitting layer, the higher the initial mixing index will be. In our particular case, $z < \theta < r$. For this reason, we normalize \bar{M}_t^{NNM} by calculating:

$$\bar{M}_t^{\text{NNM}} = \frac{\bar{M}_t^{\text{NNM}} - \bar{M}_{t_{ref}}^{\text{NNM}}}{1 - \bar{M}_{t_{ref}}^{\text{NNM}}} \quad (23)$$

3.2.2. Doucet's mixing index

Different from NNM, the method by Doucet et al. [1] does not require domain splitting. Instead, the method applies a Principal Component Analysis (PCA) [50] on the correlation between the particles' position ($\mathbf{x} \in \mathbb{R}^d$, where d stands for the number of dimensions) at a given time-step (\mathbf{x}_t) and its position at a reference time-step ($\mathbf{x}_{t_{ref}}$). The method consists of the following steps:

1. Find the correlation matrix \mathbf{C}_t given $C_{t,ij} = \rho(\mathbf{x}_{t,i}, \mathbf{x}_{t_{ref},j}), \forall i, \forall j$;
2. Compute $\mathbf{B}_t = \mathbf{C}_t \mathbf{C}_t^T$;
3. Diagonalize \mathbf{B}_t and find its maximum eigenvalue $\lambda_t = (\boldsymbol{\lambda}_t)_{max}$;
4. Find eigenvector associated to λ_t , \mathbf{w}_t ;
5. Do the same to all t.

The more mixed particles are, the lower the correlation between the current and its position at the reference time-step and, consequently, the lower λ_t is going to be. The highest component of \mathbf{w}_t gives the direction to which the mixing is poorest.

As shown by Blais et al. [51], it is important to respect the natural coordinate system of the problem. Similar to what was done to NNM, the cylindrical coordinate system was used to represent the particles' positions. Also as in NNM, we used 10 s as the reference time (t_0) for the mixing index calculation.

To establish a comparison between NNM and Doucet's mixing index, the latter was normalized so that the index increases with mixing (contrary to Doucet et al. [1], and Blais et al. [51]).

$$\bar{M}_t^{\text{Doucet}} = 1 - \frac{\lambda_t}{\lambda_{t_{ref}}} \quad (24)$$

3.3. Interaction characteristics study

In this work, we also investigated the role of particles' interaction properties on the mixing. To do so, we simulated the liquid-solid fluidized bed dynamics varying particles' Young's modulus (Y), coefficient of restitution (e), coefficient of rolling friction (μ_r), coefficient of sliding friction (μ_f). The properties were varied individually while the others are kept constant (e.g. when μ_f varies from the one presented in Table 2, e , Y , and μ_r are equal to those in Table 2). The values for each of the properties are shown in Table 4.

Table 4: Particle properties applied to the particle interaction study.

Property	Values
Young's modulus (Y)	$\{10^5, 10^7, 10^9\}$ Pa
Coefficient of restitution (e)	$\{0.1, 0.3, 0.6, 0.9\}$
Coefficient of sliding friction (μ_f)	$\{0.1, 0.2, 0.6, 0.9\}$
Coefficient of rolling friction (μ_r)	$\{0.1, 0.2, 0.6, 0.9\}$

4. Results and Discussion

To establish comparisons among regimes, particles, and methods, the mixing time results are presented as the dimensionless number of flows through:

$$N_{\text{flows}} = (t - t_{ref}) \frac{U}{H_C} \quad (25)$$

where t_{ref} is the mixing index reference time (Table 3), U is the fluid inlet velocity, and H_C is the height of the cylinder. To avoid the influence of the initial bed expansion, all results were obtained in the fully developed pseudo-steady state. Additionally, the results of the study of the particle interaction properties can be found in the tables provided in the Supplementary Material, while in this section only the main features are presented and discussed. The data includes the number of flows through to reach 95, 90, 80, and 70% mixing

(N_{flows}^{95} , N_{flows}^{90} , N_{flows}^{80} , and N_{flows}^{70} , respectively), the maximum mixing (\bar{M}_{max}), and the maximum mixing divided by the number of flows through to reach it for each mixing index ($\bar{M}_{\text{max}}/N_{\text{flows}}^{\text{max}}$).

4.1. Mixing indices comparison

In Figure 5 we show how the mixing index evolves with respect to the number of flows through using the different methods, for the three particles, and under the highest (high) and the lowest (low) fluid inlet flow rates.

NNM and Doucet’s mixing indices reflect very different aspects of particle mixing. In NNM, we split the domain and count the neighbors originally on the opposite side, which provides a straightforward view of mixing in each direction. The method is very versatile, given that the domain split can be done in any coordinate system. Additionally, the method allows for the evaluation of individual mixing indices to each particle, having more localized responses to each of the components. Such results can point to regions in the domain where the mixing is poorer, and not only returning in a global response. It is important to state that the method is not suitable to any geometry, as splitting requires symmetry.

The main disadvantages of the method are the lack of information about the global mixing without accounting for individual direction components, and the need for a manually defined $N_{\text{neighbors}}$. Furthermore, the maximum mixing index of 1 can only be reached if the domain is split such that half of the particles lie on each side, consequently, the need for a precise split is a limitation.

Oppositely, Doucet’s method does not require splitting since particles are compared to themselves at a reference time-step only. In addition, the poorest mixing component at a time t can be determined by the eigenvector \mathbf{w}_t , which directly compares the mixing components and highlights time-dependent effects. It is a convenient and efficient approach to estimate mixing using Lagrangian information.

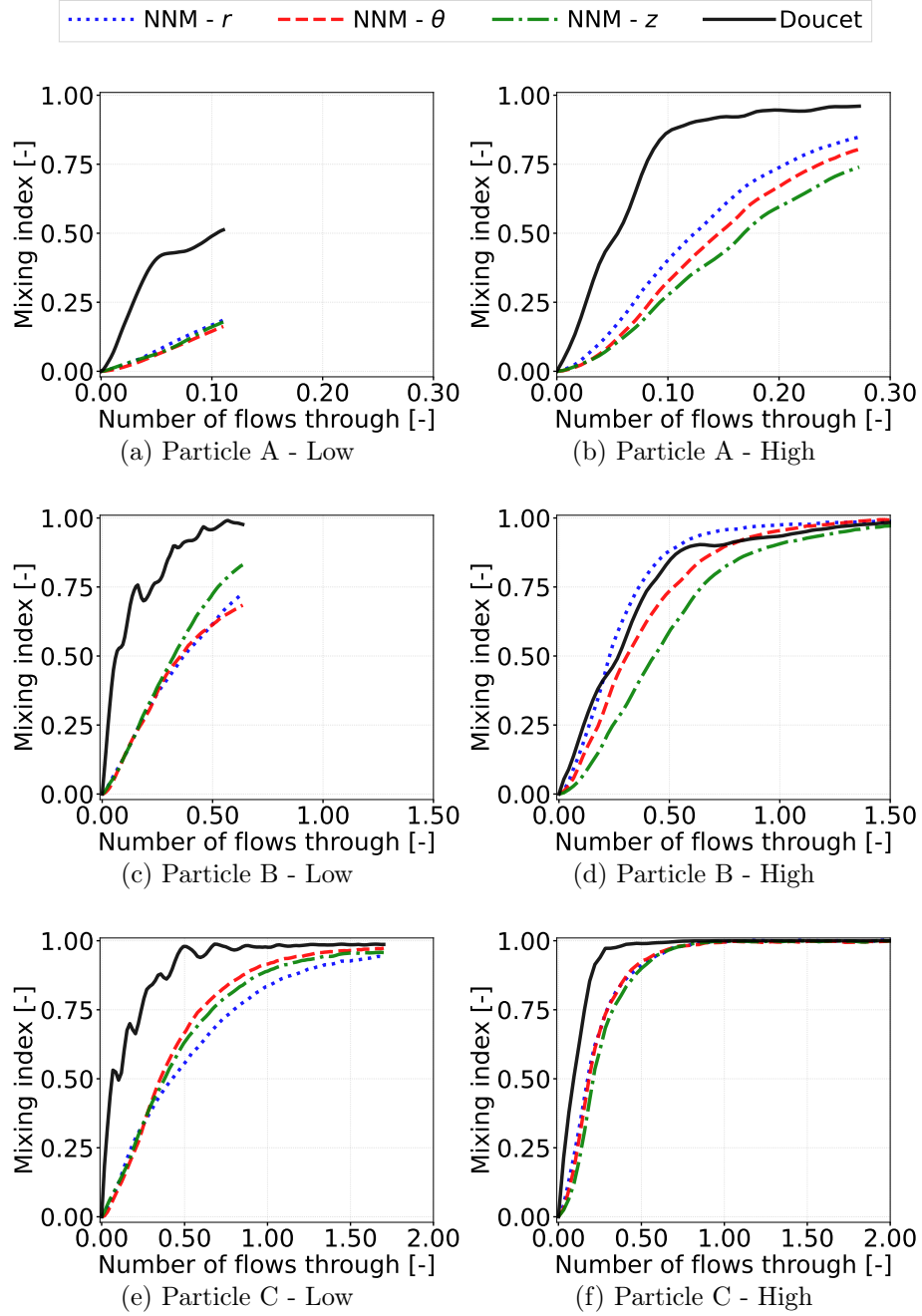


Figure 5: Mixing index as a function of N_{flows} for the three particles at lowest (low) and highest (high) fluid inlet flow rates.

4.2. Inlet flow rate

In Figures 6 and 7, we show the effect of the inlet flow rate on the mixing of particles A and C, respectively.

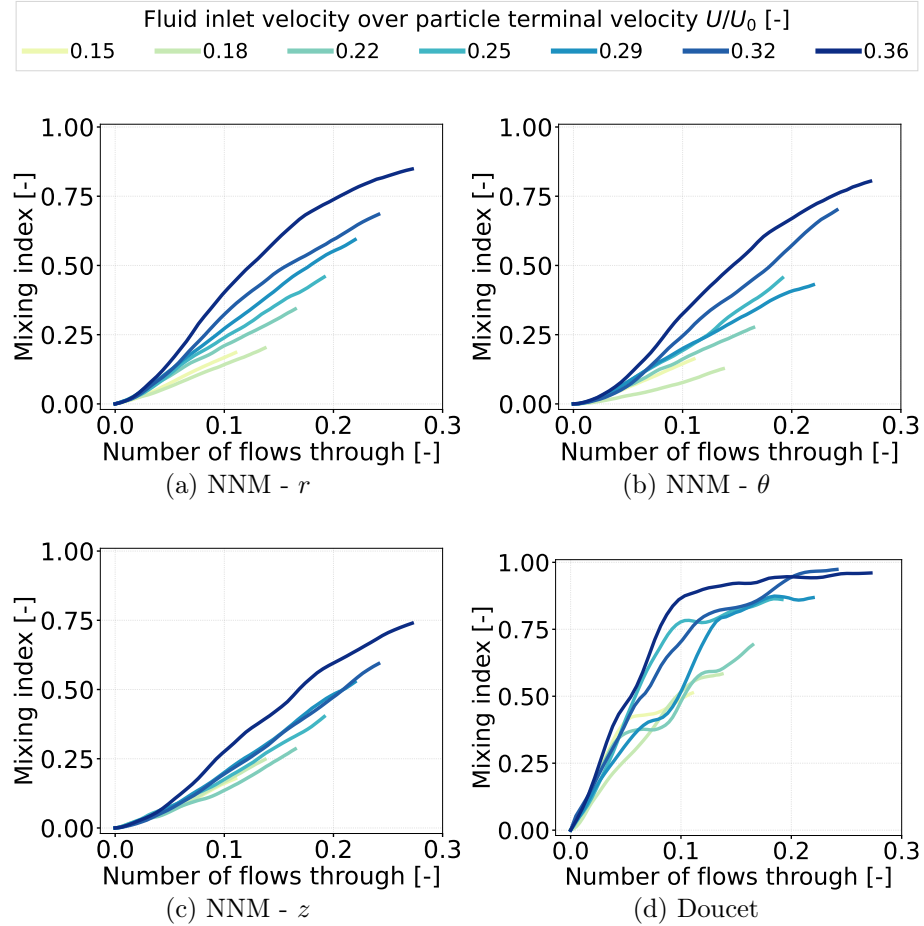


Figure 6: Mixing index as a function of time for particle A at several inlet flow rates.

It is intuitive to think that the inlet flow rate has a major impact on mixing in a fluidized bed. The higher the inlet flow rate is, the higher the particle-fluid forces are going to be, which increases particle momentum. In addition, increasing the average void fraction $\bar{\varepsilon}_f$ will increase the particles' mean free path. In other words, in theory, the mixing rate is improved because particles

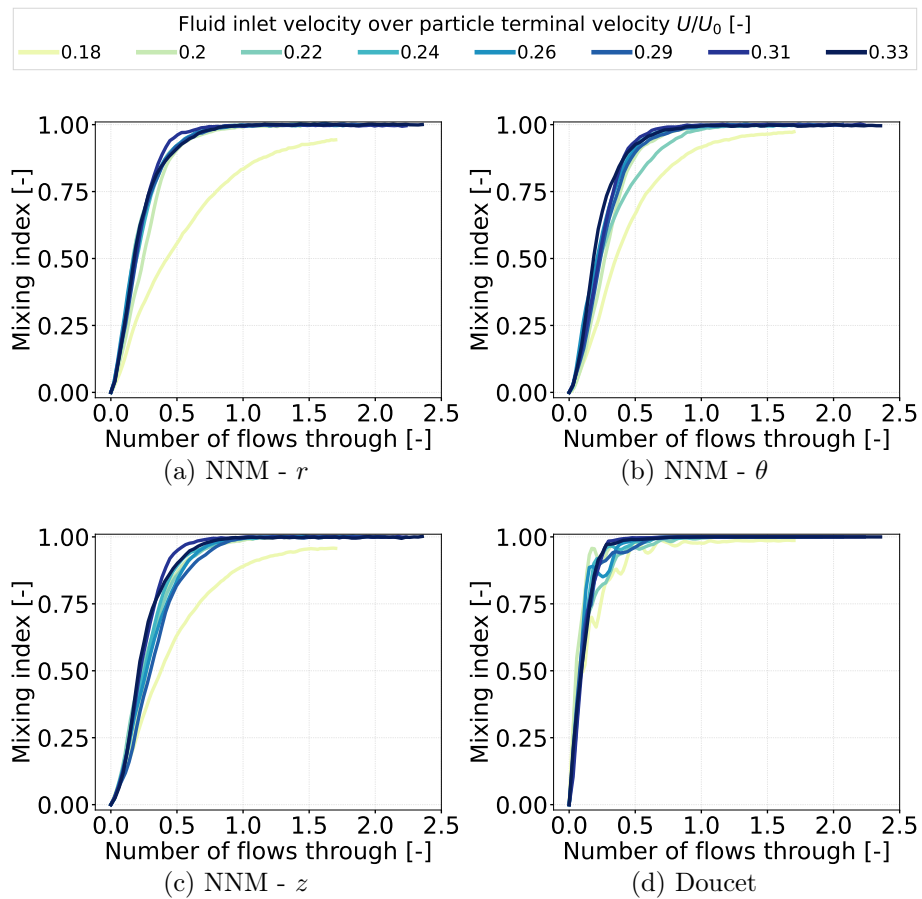


Figure 7: Mixing index as a function of time for particle C at several inlet flow rates.

move faster with less resistance due to interactions. This behavior is clearly demonstrated in the results in Figures 6 and 7. In general, cases with U/U_0 closer to 1.00 presented lower mixing times, regardless of the component.

In the case of particle A, increasing the inlet flow rate had a positive impact on mixing. For the same number of flows through, higher flow rate simulations achieved higher mixing indices than lower ones. This was observed on all indices. For instance, the mixing index was twice higher at maximum inlet flow rate compared to the minimum when the number of flows through was close to 0.1. In other words, at very low Reynolds, increasing the flow rate had a positive impact on the mixing rate.

Conversely, observing the evolution of mixing with N_{flows} , this increase seems to reach a *plateau*, as demonstrated in Figure 8. In the Figure, the number of flows through for the system to reach 90% mixing is presented as a function of the inlet flow rate.

It is not clear whether there is a gain in the mixing rate with the increase of U/U_0 . Apparently, apart from velocities very close to the minimum fluidization, the effect of the bed expansion on the evolution of mixing with the number of flows through is mild. All simulations presented very similar mixing performances, except for the very concentrate bed. Overall, in the case of particle C, there was no gain in the mixing rate when the fluid inlet velocity was increased.

The difference between regimes can be due to their difference in Stokes numbers. Particle A has a very low density. As such, Particle A responds almost immediately to differences in the fluid flow, while Particle C has a way higher inertia. This difference has an important impact on the particles' agitation in the fluidized bed. In the case of particle A, small increments in the fluid velocity reflected in a higher agitation state, while for particle C this was not the case.

4.3. Principal mixing component

Apart from the initial bed expansion, the movement of particles in a pseudo-steady state LSFb does not necessarily follow the flow direction. The resultant force acting over a particle (collisions and interphase momentum exchange)

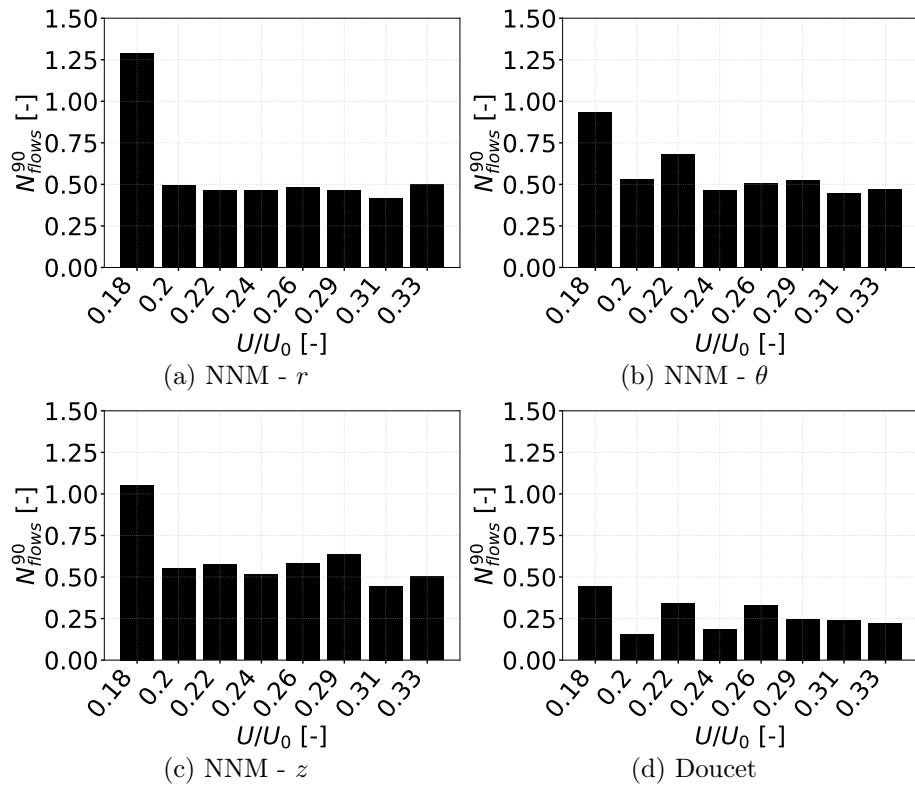


Figure 8: N_{flows}^{90} particle C at several inlet flow rates.

changes direction very frequently. Consequently, the principal mixing component given by the w_t is not the same throughout a simulation, even at a well-established pseudo-steady state.

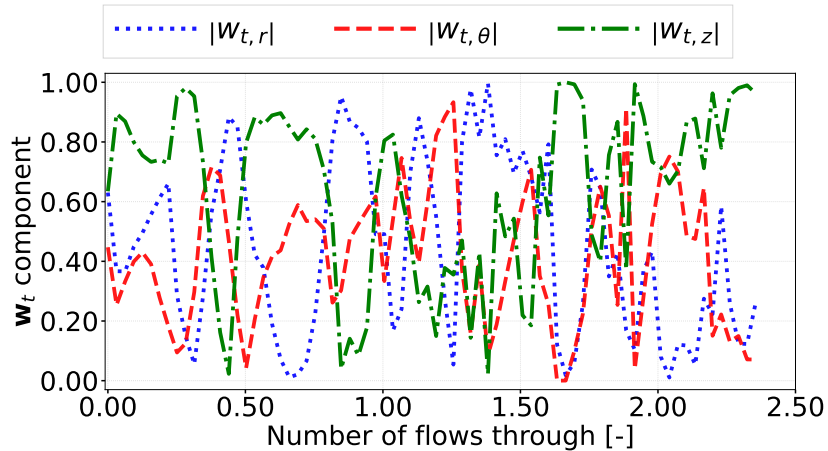


Figure 9: Main eigenvector extracted from the principal component analysis as a function of time.

In Figure 9, we show Doucet’s eigenvector analysis for particle C results for the highest inlet flow rate. From Figure 9, it can be seen that the components are not predominantly slower at all times. This behavior was observed in all simulations and particles. As such, the mixing was isotropic for all particles and regimes. A similar behavior can be observed by performing the principal component analysis on a Brownian motion system. An illustration of this PCA in a Brownian motion system is provided in the Appendix A.

4.4. Interaction properties

The discussions in this section are based on the data in the Supplementary Material. For the present analysis, we use the maximum mixing index achieved at the end of the simulation, defined as \bar{M}_{\max} , to have an assessment of the mixing level regardless of the regime. Overall, changing the particle interaction properties did not imply a significant change in the mixing behavior. We could not observe significant implications when the coefficient of restitution or the

coefficient of rolling friction were varied. The highest standard deviation among the mixing dimensionless time for the high inlet flow rate was approximately 9.2% of the average (Doucet's mixing index, N_{flows}^{95}), while \bar{M}_{max} presented a maximum standard deviation of 3.2% (NNM, component z). For the low inlet flow rate, N_{flows}^{70} was achieved by neither of the simulations (except for outliers due to oscillations in Doucet's mixing index).

The maximum standard deviation among \bar{M}_{max} was 19% (NNM, component θ). Despite the high standard deviation, the maximum NNM mixing index in this direction was too small to draw any conclusion (0.16). As for particles B and C, the interaction properties were even less influential, especially for the high inlet flow rate. It is an expected result given that fluidized beds are driven by the interphase momentum change, while collisions play a secondary role [52]. Yet, one feature can be pointed out.

As shown in Figure 10, the results for particle A at the high and low inlet flow rate, and for particle B and C at the low inlet flow rates, there is a slight, yet, monotonous decrease in the mixing performance with the increase of the coefficient of sliding friction, prominently in r for most results, and θ for the particle C. For the cases of particles B and C, the concentrated bed with slower particles facilitates longer tangential overlapping. For a very high friction coefficient, the excessive overlapping can cause a "sticking effect", virtually adding an inertial-like effect to the agglomerated particles. In the case of particle A, the very low Stokes number allows for longer overlaps such that this effect can be felt by looser beds.

This result corroborates with previous findings by Blais et al. [51] for a liquid-solid mixer. The authors report that the erosion speed is significantly decreased when lower sliding and rolling friction coefficients are applied, especially at higher impeller velocities. Still according to the authors, the pseudo-steady state suspension is not affected by the parameters. In the liquid-solid fluidized bed, the particles tend to have lower angular velocities given the multidimensional nature of their dynamics. As such, the rolling friction coefficient plays a less important part in the dynamics. On the contrary, the sliding friction coefficient

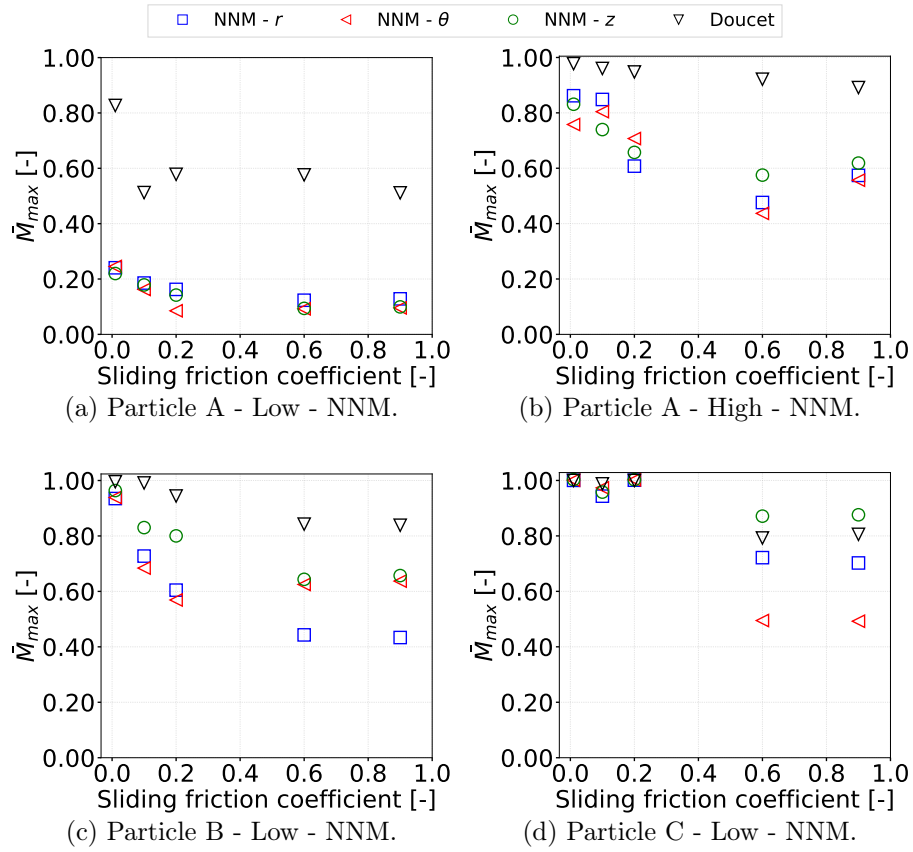


Figure 10: Scatter plots of the analysis of the principal mixing component for particles A, B, and C, with various sliding friction coefficients.

can affect the bed in a similar fashion, as it does for the transitory erosion of the particles in the mixing tank.

5. Conclusions

In the present work, we leverage the CFD-DEM model implemented in Lethé [25; 31; 43] and validated in a previous work of the research group [11] for the liquid-solid fluidized bed, using it to assess the LSFb mixing behavior. Simulations with a similar setup as the validation study were used to assess the particle dynamics inside the bed. More specifically, the method by Doucet et al. [1] and the Nearest Neighbors Method (NNM) were applied in the investigation of the bed’s mixing performance in the pseudo-steady state. The mixing evolution was expressed in terms of the number of flows through (Eq. (25)).

We demonstrate through principal component analysis that the particles mixing in the liquid-solid fluidized bed was isotropic. As mixing progresses, the eigenvectors are constantly interchanging in a random behavior, which resembles what is observed for particles following the Brownian motion pattern. The nearest neighbors method highlights the same trend, given the proximity between the indices for each of the components throughout simulations (Figure 5).

Lastly, changing the particles’ interaction properties including Young’s modulus, coefficient of restitution, coefficient of sliding friction, and coefficient of rolling friction did not have a significant effect on the mixing dynamics compared with the changes in the flow regimes. Nevertheless, the sliding friction coefficient was more influential than the other properties, especially in concentrated beds and beds with slow-moving particles. Our hypothesis is that the more concentrated the bed is, the higher the clustering provoked by the property, which results in a more prominent mixing resistance. Still, this effect vanishes for higher inlet flow rates.

6. Acknowledgments

Thanks for financial support are due to São Paulo Research Foundation (FAPESP, grant #2019/19173-9, and grant #2020/14567-6); and the Brazilian National Council for Scientific and Technological Development (CNPq, process number 408618/2018-3). The authors also thank the Federal University of São Carlos (UFSCar) and Polytechnique Montréal for the infrastructure and all the technical support. This study was financed in part by the Coordenação de Aperfeiçoamento de Pessoal de Nível Superior - Brasil (CAPES) - Finance Code 001.

We would like to acknowledge the financial support from the Natural Sciences and Engineering Research Council of Canada (NSERC) through the RGPIN-2020-04510 Discovery Grant. The authors would also like to acknowledge the technical support and computing time provided by Compute Canada and Calcul Québec.

References

- [1] J. Doucet, F. Bertrand, and J. Chaouki. A measure of mixing from Lagrangian tracking and its application to granular and fluid flow systems. *Chemical Engineering Research and Design*, 86(12):1313–1321, December 2008. doi: 10.1016/j.cherd.2008.09.003. Publisher: Elsevier BV.
- [2] Norman Epstein. Applications of Liquid-Solid Fluidization. *International Journal of Chemical Reactor Engineering*, 1(1), November 2003. doi: 10.2202/1542-6580.1010. Publisher: Walter de Gruyter GmbH.
- [3] Norman Epstein. Liquid-solids fluidization. In Wen-Ching Yang, editor, *Handbook of fluidization and fluid-particle systems*. Marcel Dekker, New York, NY, USA, 2003. ISBN 0-8247-0259-X. Section: 26.
- [4] Farhad Zamani, Jia Wei Chew, Ebrahim Akhondi, William B. Krantz, and Anthony G. Fane. Unsteady-state shear strategies to enhance mass-transfer

- for the implementation of ultrapermeable membranes in reverse osmosis: A review. *Desalination*, 356:328–348, January 2015. ISSN 00119164. doi: 10.1016/j.desal.2014.10.021. URL <https://linkinghub.elsevier.com/retrieve/pii/S001191641400544X>.
- [5] Z. Y. Zhou, S. B. Kuang, K. W. Chu, and A. B. Yu. Discrete particle simulation of particle–fluid flow: model formulations and their applicability. *Journal of Fluid Mechanics*, 661:482–510, August 2010. doi: 10.1017/s002211201000306x. Publisher: Cambridge University Press (CUP).
- [6] Ariane Bérard, Gregory S. Patience, and Bruno Blais. Experimental methods in chemical engineering: Unresolved CFD–DEM. *The Canadian Journal of Chemical Engineering*, 98(2):424–440, January 2020. doi: 10.1002/cjce.23686. Publisher: Wiley.
- [7] Alberto Di Renzo, Fernando Cello, and Francesco Paolo Di Maio. Simulation of the layer inversion phenomenon in binary liquid–fluidized beds by DEM–CFD with a drag law for polydisperse systems. *Chemical Engineering Science*, 66(13):2945–2958, July 2011. doi: 10.1016/j.ces.2011.03.035. Publisher: Elsevier BV.
- [8] Perrine Pepiot and Olivier Desjardins. Numerical analysis of the dynamics of two- and three-dimensional fluidized bed reactors using an Euler–Lagrange approach. *Powder Technology*, 220:104–121, April 2012. doi: 10.1016/j.powtec.2011.09.021. Publisher: Elsevier BV.
- [9] Bruno Blais, Manon Lassaigne, Christoph Goniva, Louis Fradette, and François Bertrand. Development of an unresolved CFD–DEM model for the flow of viscous suspensions and its application to solid–liquid mixing. *Journal of Computational Physics*, 318:201–221, August 2016. doi: 10.1016/j.jcp.2016.05.008. Publisher: Elsevier BV.
- [10] Toni El Geitani and Bruno Blais. Quadrature-Centered Averaging Scheme for Accurate and Continuous Void Fraction Calculation in Computational

Fluid Dynamics–Discrete Element Method Simulations. *Industrial & Engineering Chemistry Research*, March 2023. doi: 10.1021/acs.iecr.3c00172. Publisher: American Chemical Society (ACS).

- [11] Victor O. Ferreira, Toni El Geitani, Daniel Silva, Bruno Blais, and Gabriela C. Lopes. In-depth validation of unresolved CFD-DEM simulations of liquid fluidized beds. *Powder Technology*, 426:118652, August 2023. ISSN 00325910. doi: 10.1016/j.powtec.2023.118652. URL <https://linkinghub.elsevier.com/retrieve/pii/S0032591023004369>.
- [12] Hamid Reza Norouzi, Reza Zarghami, Rahmat Sotudeh-Gharebagh, and Navid Mostoufi. *Coupled CFD-DEM modeling: formulation, implementation and application to multiphase flows*. Wiley, Chichester, West Sussex, United Kingdom, 2016. ISBN 978-1-119-00513-1.
- [13] P. V. Danckwerts. Continuous flow systems. *Chemical Engineering Science*, 2(1):1–13, February 1953. doi: 10.1016/0009-2509(53)80001-1. Publisher: Elsevier BV.
- [14] L. T. Fan, S. J. Chen, and C. A. Watson. ANNUAL REVIEW Solids Mixing. *Industrial & Engineering Chemistry*, 62(7):53–69, July 1970. doi: 10.1021/ie50727a009. Publisher: American Chemical Society (ACS).
- [15] M. M. H. D. Arntz, W. K. den Otter, W. J. Briels, P. J. T. Bussmann, H. H. Beftink, and R. M. Boom. Granular mixing and segregation in a horizontal rotating drum: A simulation study on the impact of rotational speed and fill level. *AIChE Journal*, 54(12):3133–3146, December 2008. doi: 10.1002/aic.11622. Publisher: Wiley.
- [16] Andreas Eitzlmayr and Johannes Khinast. Co-rotating twin-screw extruders: Detailed analysis of conveying elements based on smoothed particle hydrodynamics. Part 2: Mixing. *Chemical Engineering Science*, 134:880–886, September 2015. doi: 10.1016/j.ces.2015.05.035. Publisher: Elsevier BV.

- [17] P. M. C. Lacey. Developments in the theory of particle mixing. *Journal of Applied Chemistry*, 4(5):257–268, May 1954. doi: 10.1002/jctb.5010040504. Publisher: Wiley.
- [18] Pooja Bhalode and Marianthi Ierapetritou. A review of existing mixing indices in solid-based continuous blending operations. *Powder Technology*, 373:195–209, August 2020. doi: 10.1016/j.powtec.2020.06.043. Publisher: Elsevier BV.
- [19] Victor Oliveira Ferreira, Daniel Silva Junior, Karla Raphaela Braga De Melo, Bruno Blais, and Gabriela Cantarelli Lopes. Prediction of the bed expansion of a liquid fluidized bed bioreactor applied to wastewater treatment and biogas production. *Energy Conversion and Management*, 290:117224, 2023. ISSN 01968904. doi: 10.1016/j.enconman.2023.117224. URL <https://linkinghub.elsevier.com/retrieve/pii/S0196890423005708>.
- [20] R. Escudié, Norman Epstein, John R. Grace, and H. T. Bi. Effect of particle shape on liquid-fluidized beds of binary (and ternary) solids mixtures: segregation vs. mixing. *Chemical Engineering Science*, 61(5):1528–1539, March 2006. doi: 10.1016/j.ces.2005.08.028. Publisher: Elsevier BV.
- [21] Zhengbiao Peng, Jyeshtharaj B. Joshi, Behdad Moghtaderi, Md Shakhaoath Khan, Geoffrey M. Evans, and Elham Doroodchi. Segregation and dispersion of binary solids in liquid fluidised beds: A CFD-DEM study. *Chemical Engineering Science*, 152:65–83, October 2016. doi: 10.1016/j.ces.2016.05.032. Publisher: Elsevier BV.
- [22] Md Shakhaoath Khan, Geoffrey M. Evans, Anh V. Nguyen, and Subhasish Mitra. Analysis of particle dispersion coefficient in solid-liquid fluidised beds. *Powder Technology*, 365:60–73, April 2020. doi: 10.1016/j.powtec.2019.03.022. Publisher: Elsevier BV.
- [23] Zhouzun Xie, Shuai Wang, and Yansong Shen. CFD-DEM study of segregation and mixing characteristics under a bi-disperse solid-liquid fluidised

- bed. *Advanced Powder Technology*, 32(11):4078–4095, November 2021. doi: 10.1016/j.appt.2021.09.012. Publisher: Elsevier BV.
- [24] Zhouzun Xie, Xinyu Gu, and Yansong Shen. A Machine Learning Study of Predicting Mixing and Segregation Behaviors in a Bidisperse Solid–Liquid Fluidized Bed. *Industrial & Engineering Chemistry Research*, 61(24):8551–8565, March 2022. doi: 10.1021/acs.iecr.2c00071. Publisher: American Chemical Society (ACS).
- [25] Toni El Geitani, Shahab Golshan, and Bruno Blais. A high-order stabilized solver for the volume averaged Navier-Stokes equations. *International Journal for Numerical Methods in Fluids*, February 2023. doi: 10.1002/fd.5182. Publisher: Wiley.
- [26] Toni El Geitani, Shahab Golshan, and Bruno Blais. Towards High-Order CFD-DEM: Development and Validation. *Industrial & Engineering Chemistry Research*, January 2023. doi: 10.1021/acs.iecr.2c03546. Publisher: American Chemical Society (ACS).
- [27] Toni Geitani and Bruno Blais. Solid-liquid rotary kilns: An experimental and CFD-DEM study. *Powder Technology*, page 119008, September 2023. ISSN 00325910. doi: 10.1016/j.powtec.2023.119008. URL <https://linkinghub.elsevier.com/retrieve/pii/S003259102300791X>.
- [28] Dimitri Gidaspow. *Multiphase Flow and Fluidization: Continuum and Kinetic Theory Descriptions*. Academic Press, Boston, 1994. ISBN 978-0-12-282470-8.
- [29] H. P. Zhu, Z. Y. Zhou, R. Y. Yang, and A. B. Yu. Discrete particle simulation of particulate systems: Theoretical developments. *Chemical Engineering Science*, 62(13):3378–3396, July 2007. doi: 10.1016/j.ces.2006.12.089. Publisher: Elsevier BV.
- [30] Bruno Blais, David Vidal, Francois Bertrand, Gregory S. Patience, and Jamal Chaouki. Experimental Methods in Chemical Engineering: Discrete

- Element Method—DEM. *The Canadian Journal of Chemical Engineering*, 97(7):1964–1973, June 2019. doi: 10.1002/cjce.23501. Publisher: Wiley.
- [31] Shahab Golshan, Peter Munch, Rene Gassmüller, Martin Kronbichler, and Bruno Blais. Lethe-DEM: an open-source parallel discrete element solver with load balancing. *Computational Particle Mechanics*, 10(1):77–96, May 2022. doi: 10.1007/s40571-022-00478-6. Publisher: Springer Science and Business Media LLC.
- [32] P. A. Cundall and O. D. L. Strack. A discrete numerical model for granular assemblies. *Géotechnique*, 29(1):47–65, March 1979. doi: 10.1680/geot.1979.29.1.47. Publisher: Thomas Telford Ltd.
- [33] Alberto Di Renzo and Francesco Paolo Di Maio. Homogeneous and bubbling fluidization regimes in DEM–CFD simulations: Hydrodynamic stability of gas and liquid fluidized beds. *Chemical Engineering Science*, 62(1-2):116–130, January 2007. doi: 10.1016/j.ces.2006.08.009. Publisher: Elsevier BV.
- [34] Clayton T. Crowe, John D. Schwarzkopf, Martin Sommerfeld, and Yutaka Tsuji. *Multiphase Flows with Droplets and Particles*. CRC Press, August 2011. doi: 10.1201/b11103.
- [35] R. Di Felice. The voidage function for fluid-particle interaction systems. *International Journal of Multiphase Flow*, 20(1):153–159, February 1994. doi: 10.1016/0301-9322(94)90011-6. Publisher: Elsevier BV.
- [36] R. Beetstra, M. A. van der Hoef, and J. A. M. Kuipers. Drag force of intermediate Reynolds number flow past mono- and bidisperse arrays of spheres. *AIChE Journal*, 53(2):489–501, 2007. doi: 10.1002/aic.11065. Publisher: Wiley.
- [37] Luca Mazzei and Paola Lettieri. A drag force closure for uniformly dispersed fluidized suspensions. *Chemical Engineering Science*, 62(22):6129–6142, November 2007. doi: 10.1016/j.ces.2007.06.028. Publisher: Elsevier BV.

- [38] L. W. Rong, K. J. Dong, and A. B. Yu. Lattice-Boltzmann simulation of fluid flow through packed beds of uniform spheres: Effect of porosity. *Chemical Engineering Science*, 99:44–58, August 2013. doi: 10.1016/j.ces.2013.05.036. Publisher: Elsevier BV.
- [39] Joseph Marius DallaValle. *Micromeritics: The Technology of Fine Particles*. Pitman Pub. Corp., 1948.
- [40] P. G. Saffman. The lift on a small sphere in a slow shear flow. *Journal of Fluid Mechanics*, 22(2):385–400, June 1965. doi: 10.1017/s0022112065000824. Publisher: Cambridge University Press (CUP).
- [41] P. G. Saffman. The lift on a small sphere in a slow shear flow - Corrigendum. *Journal of Fluid Mechanics*, 31(3):624–624, February 1968. doi: 10.1017/s0022112068999990. Publisher: Cambridge University Press (CUP).
- [42] R. Mei. An approximate expression for the shear lift force on a spherical particle at finite reynolds number. *International Journal of Multiphase Flow*, 18(1):145–147, January 1992. doi: 10.1016/0301-9322(92)90012-6. Publisher: Elsevier BV.
- [43] Bruno Blais, Lucka Barbeau, Valérie Bibeau, Simon Gauvin, Toni El Geitani, Shahab Golshan, Rajeshwari Kamble, Ghazaleh Mirakhori, and Jamal Chaouki. Lethe: An open-source parallel high-order adaptative CFD solver for incompressible flows. *SoftwareX*, 12:100579, July 2020. doi: 10.1016/j.softx.2020.100579. Publisher: Elsevier BV.
- [44] Daniel Arndt, Wolfgang Bangerth, Bruno Blais, Marc Fehling, Rene Gassmöller, Timo Heister, Luca Heltai, Uwe Köcher, Martin Kronbichler, Matthias Maier, Peter Munch, Jean-Paul Pelteret, Sebastian Proell, Konrad Simon, Bruno Turcksin, David Wells, and Jiaqi Zhang. The deal.II library, Version 9.3. *Journal of Numerical Mathematics*, 29(3):171–186, September 2021. doi: 10.1515/jnma-2021-0081. Publisher: Walter de Gruyter GmbH.

- [45] Daniel Arndt, Wolfgang Bangerth, Marco Feder, Marc Fehling, Rene Gassmüller, Timo Heister, Luca Heltai, Martin Kronbichler, Matthias Maier, Peter Munch, Jean-Paul Pelteret, Simon Sticko, Bruno Turcksin, and David Wells. The deal.II library, Version 9.4. *Journal of Numerical Mathematics*, 30(3):231–246, July 2022. doi: 10.1515/jnma-2022-0054. Publisher: Walter de Gruyter GmbH.
- [46] J. F. Richardson and W. N. Zaki. Sedimentation and fluidisation: Part I. *Chemical Engineering Research and Design*, 75:S82–S100, December 1954. doi: 10.1016/s0263-8762(97)80006-8. Publisher: Elsevier BV.
- [47] W. Godlieb, N. G. Deen, and J. A. M. Kuipers. Characterizing solids mixing in DEM simulations. In *6th International Conference on Multiphase Flow, ICMF 2007, Leipzig, Germany, 2007*. URL https://www.researchgate.net/profile/Niels-Deen/publication/228722534_Characterizing_solids_mixing_in_DEM_simulations/links/00b495289f429c5b39000000/Characterizing-solids-mixing-in-DEM-simulations.pdf.
- [48] C. Sullivan and Alexander Kaszynski. PyVista: 3D plotting and mesh analysis through a streamlined interface for the Visualization Toolkit (VTK). *Journal of Open Source Software*, 4(37):1450, May 2019. doi: 10.21105/joss.01450. Publisher: The Open Journal.
- [49] F. Pedregosa, G. Varoquaux, A. Gramfort, V. Michel, B. Thirion, O. Grisel, M. Blondel, P. Prettenhofer, R. Weiss, V. Dubourg, J. Vanderplas, A. Passos, D. Cournapeau, M. Brucher, M. Perrot, and E. Duchesnay. Scikit-learn: Machine Learning in Python. *Journal of Machine Learning Research*, 12: 2825–2830, 2011.
- [50] Jonathon Shlens. A Tutorial on Principal Component Analysis. *arXiv*, 2014. doi: 10.48550/ARXIV.1404.1100. URL <https://arxiv.org/abs/1404.1100>. Publisher: arXiv Version Number: 1.

- [51] Bruno Blais, Olivier Bertrand, Louis Fradette, and François Bertrand. CFD-DEM simulations of early turbulent solid–liquid mixing: Prediction of suspension curve and just-suspended speed. *Chemical Engineering Research and Design*, 123:388–406, July 2017. doi: 10.1016/j.cherd.2017.05.021. Publisher: Elsevier BV.
- [52] John Grace, Xiaotao Bi, and Naoko Ellis, editors. *Essentials of Fluidization Technology*. Wiley, 1 edition, April 2020. ISBN 978-3-527-34064-4 978-3-527-69948-3. doi: 10.1002/9783527699483. URL <https://onlinelibrary.wiley.com/doi/book/10.1002/9783527699483>.

Appendix A. Principal component analysis of Brownian motion

Let us take the Brownian motion of 25 enclosed particles in bi-dimensional (x, y) domain. Performing the analysis of the principal components of mixing, we can observe an increase in mixing with time, as shown in Figure A.11a. By definition, given enough time for particles to diffuse, the Brownian motion will lead to a well-mixed system in all directions, with no principal component. This is evident in the interchangeable behavior of Doucet's eigenvectors with time shown in Figure A.11b. In other words, the closer we are to an isotropic mixing, the less stable the eigenvectors will be.

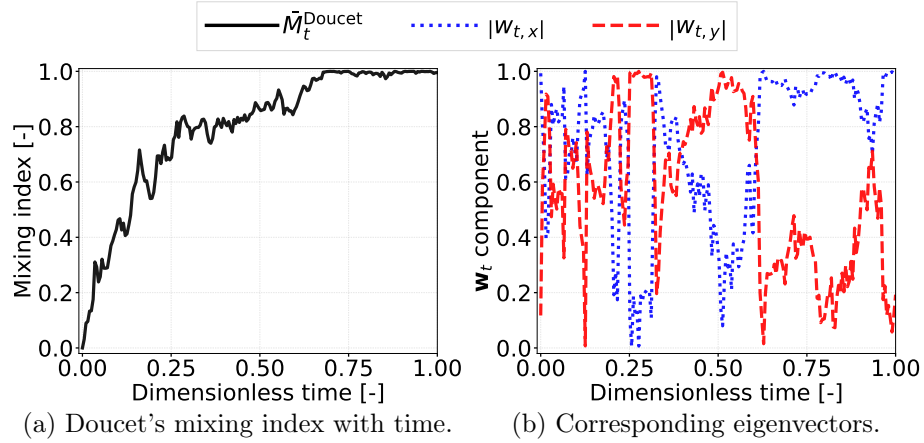


Figure A.11: Principal component analysis applied to Brownian motion.

Appendix B. Supplementary material

	$N_{flows}^{\%}$	Standard	Coefficient of restitution			Coefficient of rolling friction				Coefficient of sliding friction				Young's modulus	
			0.1	0.3	0.6	0.01	0.1	0.6	0.9	0.01	0.2	0.6	0.9	1e5	1e9
NNM - r	95%	—	—	—	—	—	—	—	—	—	—	—	—	—	—
	90%	—	—	—	—	—	—	—	—	—	—	—	—	—	—
	80%	0.234	0.261	0.250	0.256	—	0.229	0.256	0.261	0.234	—	—	—	—	—
	70%	0.185	0.207	0.207	0.201	0.229	0.185	0.207	0.223	0.196	—	—	—	—	—
	\bar{M}_{max}	0.848	0.822	0.831	0.835	0.767	0.868	0.833	0.818	0.862	0.608	0.476	0.574	0.548	—
	$\bar{M}_{max}/N_{flows}^{max}$	3.117	3.019	3.054	3.066	2.820	3.188	3.059	3.006	3.167	2.233	1.750	2.110	2.013	—
NNM - θ	95%	—	—	—	—	—	—	—	—	—	—	—	—	—	—
	90%	—	—	—	—	—	—	—	—	—	—	—	—	—	—
	80%	0.272	—	—	—	—	0.250	0.261	—	—	—	—	—	—	—
	70%	0.218	0.223	0.234	0.223	0.256	0.207	0.212	0.245	0.256	0.272	—	—	—	—
	\bar{M}_{max}	0.804	0.793	0.777	0.791	0.735	0.838	0.831	0.755	0.758	0.707	0.437	0.557	0.520	—
	$\bar{M}_{max}/N_{flows}^{max}$	2.955	2.915	2.855	2.906	2.700	3.078	3.054	2.773	2.785	2.599	1.606	2.046	1.909	—
NNM - z	95%	—	—	—	—	—	—	—	—	—	—	—	—	—	—
	90%	—	—	—	—	—	—	—	—	—	—	—	—	—	—
	80%	—	—	—	—	—	—	—	—	0.256	—	—	—	—	—
	70%	0.250	0.245	0.256	0.272	0.261	0.245	0.261	—	0.218	—	—	—	—	—
	\bar{M}_{max}	0.740	0.770	0.748	0.704	0.732	0.765	0.728	0.682	0.831	0.657	0.575	0.619	0.674	—
	$\bar{M}_{max}/N_{flows}^{max}$	2.718	2.829	2.749	2.586	2.688	2.810	2.677	2.504	3.054	2.415	2.113	2.273	2.477	—
Doucet	95%	0.239	—	0.191	0.212	—	0.212	0.191	0.223	0.234	—	—	—	0.239	—
	90%	0.125	0.125	0.109	0.131	0.212	0.114	0.174	0.191	0.180	0.158	0.239	—	0.163	—
	80%	0.087	0.082	0.082	0.082	0.147	0.093	0.136	0.136	0.109	0.136	0.191	0.163	0.142	—
	70%	0.076	0.071	0.071	0.065	0.054	0.076	0.098	0.076	0.076	0.120	0.152	0.136	0.131	—
	\bar{M}_{max}	0.960	0.934	0.983	0.984	0.946	0.977	0.981	0.966	0.978	0.948	0.922	0.891	0.968	—
	$\bar{M}_{max}/N_{flows}^{max}$	3.529	3.431	3.612	3.617	3.696	3.591	3.606	3.551	3.592	3.482	3.762	3.275	3.630	—

Table B.5: Particle A - High inlet velocity.

	$N_{flows}^{\%}$	Standard	Coefficient of restitution			Coefficient of rolling friction				Coefficient of sliding friction				Young's modulus	
			0.1	0.3	0.6	0.01	0.1	0.6	0.9	0.01	0.2	0.6	0.9	1e5	1e9
NNM - r	95%	—	—	—	—	—	—	—	—	—	—	—	—	—	—
	90%	—	—	—	—	—	—	—	—	—	—	—	—	—	—
	80%	—	—	—	—	—	—	—	—	—	—	—	—	—	—
	70%	—	—	—	—	—	—	—	—	—	—	—	—	—	—
	\bar{M}_{max}	0.185	0.173	0.184	0.187	0.199	0.187	0.180	0.179	0.241	0.163	0.123	0.128	0.145	—
$\bar{M}_{max}/N_{flows}^{max}$	1.680	1.571	1.670	1.698	1.801	1.697	1.635	1.688	2.181	1.473	1.118	1.163	1.318	—	
NNM - θ	95%	—	—	—	—	—	—	—	—	—	—	—	—	—	—
	90%	—	—	—	—	—	—	—	—	—	—	—	—	—	—
	80%	—	—	—	—	—	—	—	—	—	—	—	—	—	—
	70%	—	—	—	—	—	—	—	—	—	—	—	—	—	—
	\bar{M}_{max}	0.162	0.096	0.116	0.125	0.182	0.145	0.138	0.151	0.245	0.085	0.092	0.096	0.050	—
$\bar{M}_{max}/N_{flows}^{max}$	1.472	0.866	1.053	1.135	1.648	1.310	1.254	1.421	2.224	0.772	0.836	0.867	0.451	—	
NNM - z	95%	—	—	—	—	—	—	—	—	—	—	—	—	—	—
	90%	—	—	—	—	—	—	—	—	—	—	—	—	—	—
	80%	—	—	—	—	—	—	—	—	—	—	—	—	—	—
	70%	—	—	—	—	—	—	—	—	—	—	—	—	—	—
	\bar{M}_{max}	0.179	0.167	0.167	0.170	0.208	0.178	0.174	0.170	0.220	0.142	0.094	0.099	0.171	—
$\bar{M}_{max}/N_{flows}^{max}$	1.619	1.516	1.512	1.537	1.889	1.615	1.580	1.607	1.992	1.286	0.851	0.900	1.549	—	
Doucet	95%	—	—	—	—	—	—	—	—	—	—	—	—	—	—
	90%	—	—	—	—	—	—	—	—	—	—	—	—	—	—
	80%	—	—	—	—	—	—	—	—	0.090	—	—	—	—	—
	70%	—	—	—	—	—	—	—	—	0.068	—	—	—	—	—
	\bar{M}_{max}	0.512	0.578	0.531	0.560	0.638	0.533	0.559	0.556	0.827	0.578	0.576	0.511	0.460	—
$\bar{M}_{max}/N_{flows}^{max}$	4.643	9.351	4.815	5.071	5.777	4.830	5.066	5.251	7.807	5.241	5.222	4.634	4.165	—	

Table B.6: Particle A - Low inlet velocity.

	$N_{flows}^{\%}$	Standard	Coefficient of restitution			Coefficient of rolling friction				Coefficient of sliding friction				Young's modulus	
			0.1	0.3	0.6	0.01	0.1	0.6	0.9	0.01	0.2	0.6	0.9	1e5	1e9
NNM - r	95%	0.726	0.682	0.682	0.594	0.704	0.660	0.748	0.660	0.726	0.660	0.616	0.836	0.660	—
	90%	0.550	0.550	0.550	0.484	0.550	0.528	0.616	0.550	0.594	0.528	0.484	0.660	0.572	—
	80%	0.418	0.418	0.418	0.374	0.418	0.418	0.484	0.418	0.440	0.396	0.374	0.484	0.440	—
	70%	0.330	0.352	0.330	0.308	0.330	0.330	0.374	0.330	0.352	0.330	0.308	0.396	0.374	—
	\bar{M}_{max}	0.993	1.000	0.997	1.000	1.000	1.000	0.997	1.000	1.000	1.000	1.000	1.000	0.994	0.996
NNM - θ	$\bar{M}_{max}/N_{flows}^{max}$	0.602	0.623	0.731	0.631	0.688	0.689	0.604	0.689	0.606	0.606	0.640	0.619	0.686	—
	95%	0.968	0.770	0.858	0.748	0.704	0.704	0.946	0.902	0.748	0.814	0.814	0.902	0.748	—
	90%	0.770	0.638	0.682	0.638	0.594	0.550	0.704	0.682	0.594	0.660	0.660	0.748	0.616	—
	80%	0.594	0.484	0.506	0.484	0.462	0.440	0.528	0.506	0.462	0.506	0.506	0.572	0.506	—
	70%	0.484	0.418	0.396	0.374	0.374	0.352	0.418	0.418	0.374	0.418	0.418	0.462	0.418	—
NNM - z	\bar{M}_{max}	0.998	0.999	0.997	0.999	1.000	0.999	0.995	1.000	1.000	1.000	0.999	0.998	1.000	—
	$\bar{M}_{max}/N_{flows}^{max}$	0.622	0.605	0.604	0.606	0.710	0.614	0.603	0.649	0.614	0.622	0.640	0.639	0.699	—
	95%	1.298	1.386	1.056	0.792	0.880	1.056	1.474	1.166	1.034	0.968	0.968	1.364	1.276	—
	90%	0.990	1.122	0.924	0.682	0.748	0.814	1.210	0.924	0.858	0.814	0.792	1.122	1.078	—
	80%	0.726	0.858	0.748	0.550	0.594	0.638	0.924	0.660	0.704	0.616	0.594	0.880	0.836	—
Doucet	70%	0.616	0.726	0.616	0.462	0.484	0.528	0.770	0.528	0.616	0.506	0.506	0.748	0.682	—
	\bar{M}_{max}	0.983	0.983	0.997	1.000	1.000	0.990	0.964	0.994	0.999	1.000	0.997	0.990	0.990	—
	$\bar{M}_{max}/N_{flows}^{max}$	0.596	0.596	0.657	0.770	0.649	0.616	0.592	0.611	0.614	0.622	0.604	0.600	0.600	—
	95%	1.122	1.056	0.814	0.308	0.396	0.770	1.144	1.056	0.462	0.528	0.528	1.034	0.814	—
	90%	0.616	0.770	0.638	0.264	0.330	0.528	0.924	0.770	0.440	0.440	0.374	0.858	0.726	—
Doucet	80%	0.462	0.528	0.396	0.198	0.286	0.352	0.550	0.418	0.396	0.286	0.286	0.528	0.550	—
	70%	0.374	0.440	0.286	0.176	0.242	0.286	0.374	0.220	0.352	0.242	0.220	0.396	0.396	—
	\bar{M}_{max}	0.991	0.993	0.999	1.000	1.000	0.998	0.986	0.998	1.000	1.000	0.999	0.999	0.997	—
	$\bar{M}_{max}/N_{flows}^{max}$	0.601	0.602	0.606	0.640	0.710	0.605	0.623	0.605	0.606	0.623	0.605	0.622	0.604	—

Table B.7: Particle B - High inlet velocity.

	$N_{flows}^{\%}$	Standard	Coefficient of restitution			Coefficient of rolling friction				Coefficient of sliding friction				Young's modulus	
			0.1	0.3	0.6	0.01	0.1	0.6	0.9	0.01	0.2	0.6	0.9	1e5	1e9
NNM - r	95%	—	—	—	—	—	0.611	—	—	—	—	—	—	—	—
	90%	—	—	—	—	0.492	0.586	—	—	0.560	—	—	—	—	—
	80%	—	—	—	—	0.357	0.577	—	—	0.433	—	—	—	0.603	—
	70%	0.603	—	—	0.586	0.306	0.509	—	0.603	0.357	—	—	—	0.475	—
	$\bar{M}_{max}/N_{flows}^{max}$	0.727	0.665	0.688	0.741	0.941	0.976	0.675	0.726	0.935	0.605	0.443	0.434	0.830	—
NNM - θ	95%	—	—	—	—	—	—	—	—	—	—	—	—	—	—
	90%	—	—	—	—	0.509	0.620	—	—	0.552	—	—	—	—	—
	80%	—	—	—	—	0.382	0.577	—	—	0.441	—	—	—	—	—
	70%	—	—	—	0.577	0.340	0.560	—	0.577	0.373	—	—	—	0.560	—
	$\bar{M}_{max}/N_{flows}^{max}$	0.684	0.644	0.602	0.736	0.944	0.936	0.633	0.745	0.939	0.569	0.625	0.637	0.762	—
NNM - z	95%	—	—	—	—	—	0.611	—	—	0.603	—	—	—	—	—
	90%	—	—	—	—	—	0.586	—	—	0.509	—	—	—	—	—
	80%	0.594	0.594	0.594	0.594	0.518	0.569	0.577	0.628	0.416	0.637	—	—	0.594	—
	70%	0.484	0.475	0.467	0.475	0.416	0.484	0.467	0.492	0.357	0.560	—	—	0.467	—
	$\bar{M}_{max}/N_{flows}^{max}$	0.830	0.826	0.833	0.821	0.864	0.972	0.843	0.808	0.964	0.800	0.644	0.657	0.831	—
Doucet	95%	1.304	1.298	1.309	1.289	1.357	1.527	1.324	1.269	1.514	1.257	1.011	1.032	1.306	—
	90%	0.450	0.467	0.475	0.475	0.212	0.577	0.441	0.450	0.289	—	—	—	0.501	—
	80%	0.365	0.424	0.424	0.357	0.195	0.314	0.399	0.340	0.246	0.552	—	—	0.280	—
	70%	0.280	0.289	0.306	0.272	0.153	0.255	0.297	0.263	0.161	0.433	0.603	0.586	0.212	—
	$\bar{M}_{max}/N_{flows}^{max}$	0.136	0.229	0.238	0.212	0.102	0.119	0.229	0.127	0.127	0.331	0.450	0.475	0.170	—
		0.991	0.979	0.981	0.981	0.997	0.989	0.976	0.989	0.996	0.944	0.843	0.839	0.968	—
		1.743	1.537	1.778	1.628	1.836	1.554	1.576	1.792	1.564	1.483	1.324	1.317	1.521	—

Table B.8: Particle B - Low inlet velocity.

	$N_{flows}^{\%}$	Standard	Coefficient of restitution			Coefficient of rolling friction				Coefficient of sliding friction				Young's modulus	
			0.1	0.3	0.6	0.01	0.1	0.6	0.9	0.01	0.2	0.6	0.9	1e5	1e9
NNM - r	95%	0.628	0.534	0.565	0.565	0.534	0.597	0.628	0.534	0.565	0.534	0.785	0.597	0.597	0.534
	90%	0.503	0.440	0.471	0.503	0.471	0.503	0.503	0.408	0.471	0.440	0.628	0.471	0.503	0.408
	80%	0.345	0.377	0.377	0.408	0.377	0.377	0.408	0.314	0.345	0.345	0.471	0.377	0.377	0.345
	70%	0.283	0.314	0.314	0.314	0.314	0.314	0.345	0.251	0.283	0.283	0.377	0.314	0.314	0.283
	$\bar{M}_{max}/N_{flows}^{max}$	1.000	1.000	1.000	1.000	1.000	1.000	1.000	1.000	1.000	1.000	1.000	1.000	1.000	1.000
NNM - θ	95%	0.468	0.601	0.816	0.482	0.430	0.777	0.442	0.612	0.637	0.692	0.522	0.624	0.650	0.692
	90%	0.597	0.503	0.503	0.565	0.565	0.628	0.660	0.597	0.503	0.534	0.911	0.628	0.534	0.628
	80%	0.471	0.440	0.440	0.503	0.471	0.534	0.565	0.503	0.408	0.440	0.754	0.503	0.440	0.534
	70%	0.345	0.345	0.345	0.377	0.377	0.440	0.471	0.377	0.314	0.314	0.597	0.377	0.345	0.408
	$\bar{M}_{max}/N_{flows}^{max}$	0.283	0.283	0.283	0.314	0.345	0.377	0.408	0.283	0.251	0.283	0.503	0.314	0.283	0.345
NNM - z	95%	1.000	1.000	1.000	1.000	1.000	1.000	1.000	1.000	1.000	1.000	1.000	1.000	1.000	1.000
	90%	0.498	0.514	0.430	0.724	0.579	0.724	0.468	0.475	0.816	0.579	0.461	0.498	0.590	0.861
	80%	0.628	0.565	0.565	0.597	0.628	0.660	0.628	0.722	0.597	0.628	0.848	0.660	0.565	0.628
	70%	0.503	0.471	0.471	0.534	0.534	0.534	0.534	0.597	0.503	0.503	0.691	0.565	0.471	0.534
	$\bar{M}_{max}/N_{flows}^{max}$	0.377	0.408	0.408	0.440	0.440	0.440	0.440	0.471	0.408	0.440	0.534	0.440	0.377	0.440
Doucet	95%	0.314	0.345	0.345	0.377	0.377	0.345	0.377	0.377	0.345	0.377	0.440	0.377	0.314	0.377
	90%	1.000	1.000	1.000	1.000	1.000	1.000	1.000	1.000	1.000	1.000	1.000	1.000	1.000	1.000
	80%	0.425	0.663	0.677	0.758	0.482	0.601	0.724	0.677	0.796	0.637	0.590	0.540	0.430	0.777
	70%	0.283	0.251	0.314	0.377	0.377	0.471	0.440	0.408	0.251	0.283	0.534	0.377	0.283	0.345
	$\bar{M}_{max}/N_{flows}^{max}$	0.220	0.220	0.283	0.220	0.283	0.314	0.377	0.251	0.220	0.251	0.440	0.314	0.251	0.283
Doucet	90%	0.188	0.188	0.220	0.157	0.220	0.188	0.188	0.188	0.188	0.220	0.345	0.220	0.188	0.220
	80%	0.157	0.157	0.188	0.126	0.220	0.157	0.157	0.157	0.157	0.188	0.188	0.188	0.188	0.188
	70%	1.000	1.000	1.000	1.000	1.000	1.000	1.000	1.000	1.000	1.000	1.000	1.000	1.000	1.000
	95%	0.692	0.740	0.624	0.531	0.677	0.590	0.637	0.590	0.442	0.475	0.514	0.663	0.448	0.637
	$\bar{M}_{max}/N_{flows}^{max}$	0.692	0.740	0.624	0.531	0.677	0.590	0.637	0.590	0.442	0.475	0.514	0.663	0.448	0.637

Table B.9: Particle C - High inlet velocity.

	$N_{flows}^{\%}$	Standard	Coefficient of restitution			Coefficient of rolling friction				Coefficient of sliding friction				Young's modulus	
			0.1	0.3	0.6	0.01	0.1	0.6	0.9	0.01	0.2	0.6	0.9	1e5	1e9
NNM - r	95%	—	1.292	—	—	1.071	1.343	—	1.632	0.646	0.969	—	—	1.173	1.530
	90%	1.292	1.258	1.360	1.275	0.833	1.020	1.360	1.241	0.527	0.935	—	—	0.850	1.224
	80%	0.918	0.969	0.986	0.935	0.595	0.748	0.969	0.901	0.391	0.918	—	—	0.629	0.918
	70%	0.714	0.748	0.782	0.765	0.493	0.629	0.782	0.714	0.306	0.867	1.513	1.700	0.544	0.731
	\bar{M}_{max}	0.943	0.998	0.934	0.945	0.982	0.976	0.943	0.956	1.000	1.000	0.722	0.702	0.984	1.000
NNM - θ	$\bar{M}_{max}/N_{flows}^{max}$	0.566	0.631	0.549	0.556	0.590	0.574	0.555	0.562	0.520	0.668	0.451	0.413	0.597	0.429
	95%	1.258	1.190	1.683	1.326	1.173	1.598	1.122	1.343	0.731	0.935	—	—	1.122	1.258
	90%	0.935	0.935	1.156	0.969	0.901	1.292	0.901	1.054	0.595	0.901	—	—	0.884	0.986
	80%	0.697	0.697	0.799	0.714	0.697	0.799	0.697	0.765	0.442	0.714	—	—	0.629	0.731
	70%	0.544	0.561	0.612	0.578	0.544	0.595	0.561	0.595	0.340	0.578	—	—	0.527	0.578
NNM - z	\bar{M}_{max}	0.973	1.000	0.950	0.968	0.978	0.961	0.975	0.971	1.000	1.000	0.495	0.492	0.989	1.000
	$\bar{M}_{max}/N_{flows}^{max}$	0.572	0.653	0.564	0.575	0.587	0.565	0.573	0.571	0.442	0.653	0.310	0.290	0.582	0.463
	95%	1.428	1.292	1.615	1.700	1.394	1.496	1.632	1.700	0.782	0.952	—	—	1.241	1.632
	90%	1.054	1.156	1.088	1.122	1.105	1.071	1.054	1.224	0.663	0.935	—	—	0.969	1.241
	80%	0.765	0.799	0.782	0.799	0.748	0.748	0.731	0.816	0.544	0.833	1.054	1.037	0.680	0.816
Doucet	70%	0.595	0.612	0.629	0.612	0.544	0.595	0.578	0.612	0.425	0.629	0.765	0.765	0.544	0.612
	\bar{M}_{max}	0.958	1.000	0.956	0.951	0.974	0.967	0.952	0.951	1.000	1.000	0.871	0.876	0.984	1.000
	$\bar{M}_{max}/N_{flows}^{max}$	0.569	0.588	0.568	0.559	0.579	0.569	0.560	0.559	0.507	0.700	0.545	0.515	0.590	0.470
	95%	0.459	0.629	0.629	0.629	0.323	0.459	0.510	0.476	0.357	0.833	—	—	0.442	0.476
	90%	0.442	0.442	0.425	0.442	0.289	0.340	0.459	0.340	0.170	0.595	—	—	0.323	0.442
Doncet	80%	0.272	0.272	0.323	0.323	0.170	0.255	0.340	0.255	0.136	0.476	—	1.632	0.238	0.255
	70%	0.238	0.238	0.255	0.272	0.136	0.221	0.255	0.153	0.102	0.374	0.850	1.088	0.221	0.170
	\bar{M}_{max}	0.988	1.000	0.987	0.986	0.999	0.997	0.987	0.994	1.000	1.000	0.793	0.806	0.999	1.000
	$\bar{M}_{max}/N_{flows}^{max}$	1.452	0.588	0.611	1.137	0.587	0.604	0.611	0.596	0.452	0.606	0.496	0.483	0.816	0.414

Table B.10: Particle C - Low inlet velocity.